

Applications of computation in acoustics: Ultrasound bioeffects and transmission loss uncertainty

Brandon Patterson

Scientific Computing and Flow Physics Lab

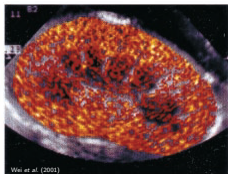
University of Michigan, Ann Arbor

¹Department of Mechanical Engineering

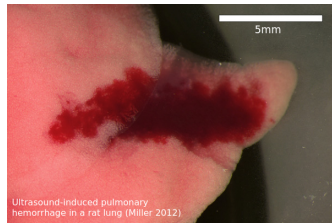
March 9, 2017

Part I: Diagnostic ultrasound bioeffects

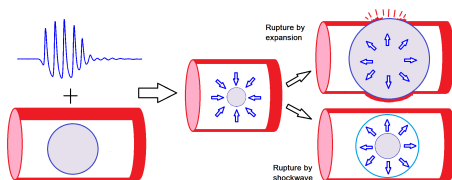
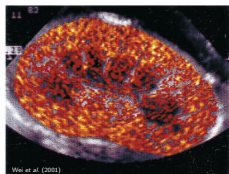
Contrast-enhanced ultrasound



Ultrasound-induced lung hemorrhage



Background on contrast-enhanced ultrasound bioeffects



- Contrast-Ehanced Ultrasound (CEUS) provides high contrast diagnostic medical imaging in areas without high contrast (e.g., blood).
- CEUS uses echogenic microbubbles for contrast, and can lead to hemorrhage and cell death.
- Though cavitation of the microbubbles appears to be the cause, the exact mechanisms and thresholds are not well understood.

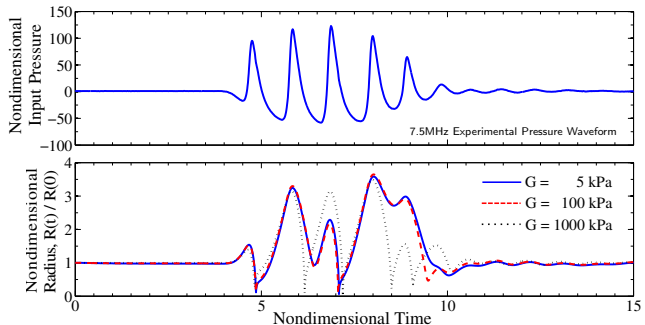
A model for spherical bubble dynamics in tissue, treated as a compressible, Voigt viscoelastic medium, was developed

$$\left(1 - \frac{\dot{R}}{C}\right) R \ddot{R} + \frac{3}{2} \left(1 - \frac{\dot{R}}{3C}\right) \dot{R}^2 = \left(1 + \frac{\dot{R}}{C}\right) \left[p_B - 1 - p_a - \frac{R}{C} \frac{dp_a}{dt} \right] + \frac{R}{C} \dot{p}_B$$
$$p_B = \left(1 + \frac{2}{We}\right) \frac{1}{R^{3\gamma}} - \frac{2}{WeR} + \tau_R$$

Parameter	Dimensional value		Dimensionless number
Viscosity	$\mu = 0.015 \text{ (Pa s)}$	\mapsto	$Re = \rho u R_o / \mu = 2/3$
Elasticity	$G = 10^5 \text{ (Pa)}$	\mapsto	$Ca = \rho u^2 / G = 1.0$
Surface tension	$S = 0.056 \text{ (N/m)}$	\mapsto	$We = \rho u^2 R_o / S = 2$
Sound speed	$c = 1570 \text{ (m/s)}$	\mapsto	$C = c/u = 157$

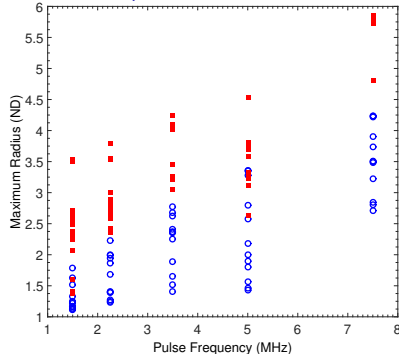
Yang, X., & Church, C. C. (2005). A model for the dynamics of gas bubbles in soft tissue. The Journal of the Acoustical Society of America, 118(6), 3595–3606.

ultrasound pulses with known occurrence of bioeffects (Miller *et al.*, 2008)

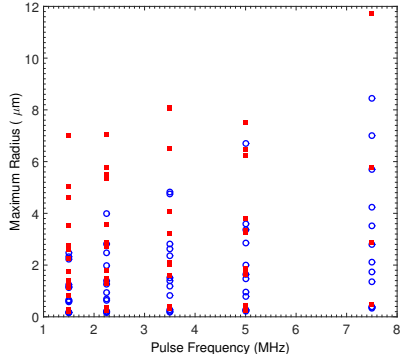


Patterson, B., Miller, D. L., & Johnsen, E. (2012). Theoretical microbubble dynamics in a viscoelastic medium at capillary breaching thresholds. JASA, 132(6), 3770.

Accepted inertial cavitation thresholds are compared with experimentally observed bioeffects thresholds



(a) R_{max}/R_0



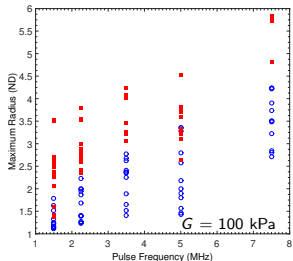
(b) R_{max}

Dependence of the bubble dynamics on the frequency for $G = 100 \text{ kPa}$.

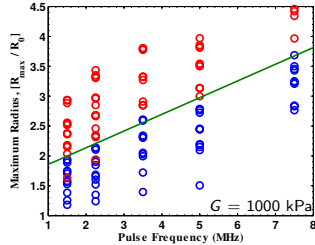
$R_0 = 0.1 - 2 \mu\text{m}$; empty circles: no bioeffects; squares: bioeffects.

- The dimensionless maximum radius, a cavitation metric appears to correlate with bioeffects. The dimensional maximum radius does not.
- Inertial cavitation threshold $R_{max}/R_0 \geq 2$ does not hold for bioeffects.

Cavitation dynamics and bioeffects thresholds strongly depend on frequency and elasticity



(a) $G = 100 \text{ kPa}$



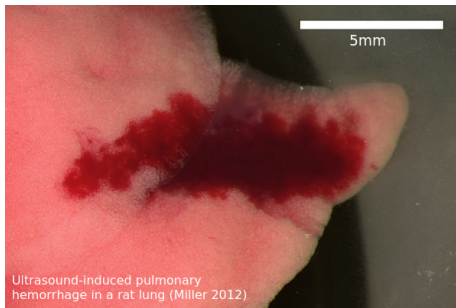
(b) $G = 1000 \text{ kPa}$

The dimensionless maximum bubble radius is plotted as a function of frequency for media of elastic moduli $G = 100, 1000 \text{ kPa}$. Marker color indicates whether corresponding experiments observed bioeffects (red) and no bioeffects (blue).

- At a given frequency, the bioeffects threshold shows a strong correlation to cavitation dynamics
- Distinction becomes more clear for more elastic media

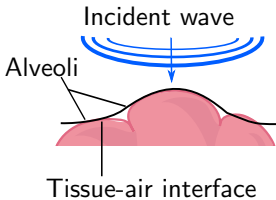
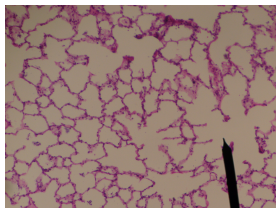
DUS-induced lung hemorrhage is not a new problem

- Lung Hemorrhage (LH) is the only known bioeffect of non-contrast DUS
- Has been shown to occur in mice, rats, pigs, rabbits, monkeys (Child *et al.*, 1990; O'Brien & Zachary, 1997; Tarantal & Canfield, 1994).
- DUS-induced LH does not appear to be a result of cavitation or heating.
- The underlying physical damage mechanism is not understood.

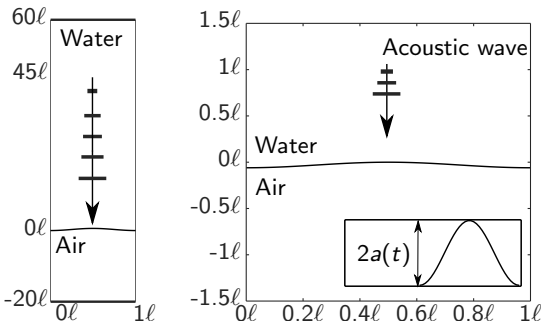


The basic physical problem we have in the lungs is a mechanical wave interacting with an air-tissue interface.

A model of ultrasound-pulse driven alveoli was developed



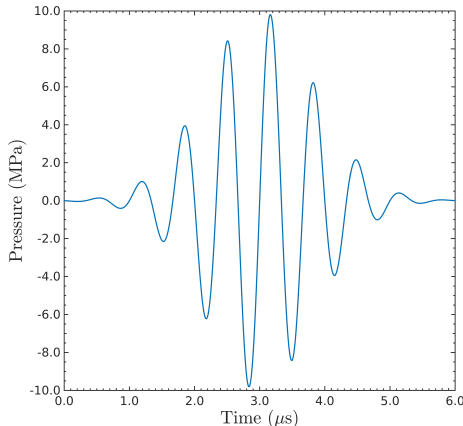
(a) Physical problem schematic



(b) Domain and model problem schematic.

A model of ultrasound-pulse driven alveoli was developed

$$p(y, t_0) = p_a \sin \left(2\pi f \frac{[y - (Y_{wave} + L_{wave})]}{c} \right) \exp \left(-\frac{\left([y - (Y_{wave} + L_{wave}/2)] c \right)^2}{FWHM / (2\sqrt{2 \ln(2)})} \right).$$



(a) Ultrasound pulse waveform

Governing Equations

Euler equations of fluid motion

$$\frac{\partial \rho}{\partial t} + \frac{\partial (\rho u)}{\partial x} + \frac{\partial (\rho v)}{\partial y} = 0,$$

$$\frac{\partial \rho u}{\partial t} + \frac{\partial}{\partial x} \left(\rho u^2 + p \right) + \frac{\partial}{\partial y} (\rho uv) = 0,$$

$$\frac{\partial \rho v}{\partial t} + \frac{\partial}{\partial x} (\rho uv) + \frac{\partial}{\partial y} \left(\rho v^2 + p \right) = 0,$$

$$\frac{\partial E}{\partial t} + \frac{\partial}{\partial x} [u(E + p)] + \frac{\partial}{\partial y} [v(E + p)] = 0,$$

Stiffened equation of state

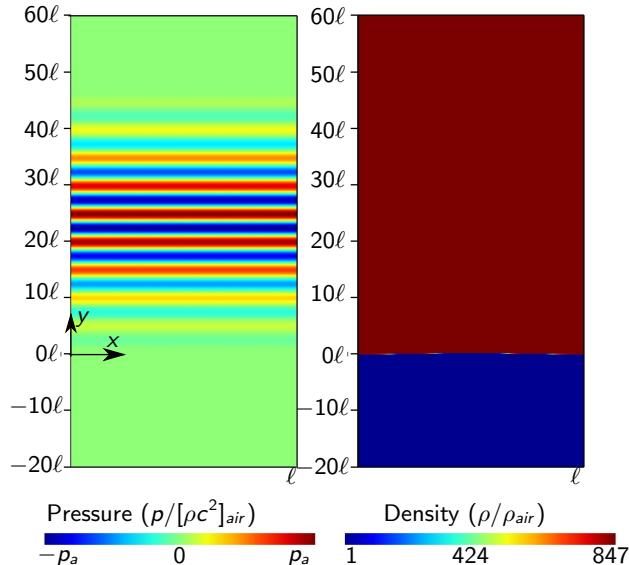
$$E = \frac{\rho(u^2 + v^2)}{2} + \frac{p + \gamma B}{\gamma - 1}.$$

Advection equations for γ, B prevent interface pressure oscillations.

$$\frac{\partial}{\partial t} \left(\frac{\gamma B}{\gamma - 1} \right) + u \frac{\partial}{\partial x} \left(\frac{\gamma B}{\gamma - 1} \right) + v \frac{\partial}{\partial y} \left(\frac{\gamma B}{\gamma - 1} \right) = 0,$$

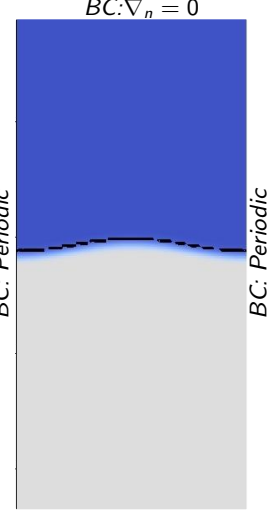
$$\frac{\partial}{\partial t} \left(\frac{1}{\gamma - 1} \right) + u \frac{\partial}{\partial x} \left(\frac{1}{\gamma - 1} \right) + v \frac{\partial}{\partial y} \left(\frac{1}{\gamma - 1} \right) = 0$$

The model provides our initial condition for the Euler Equations



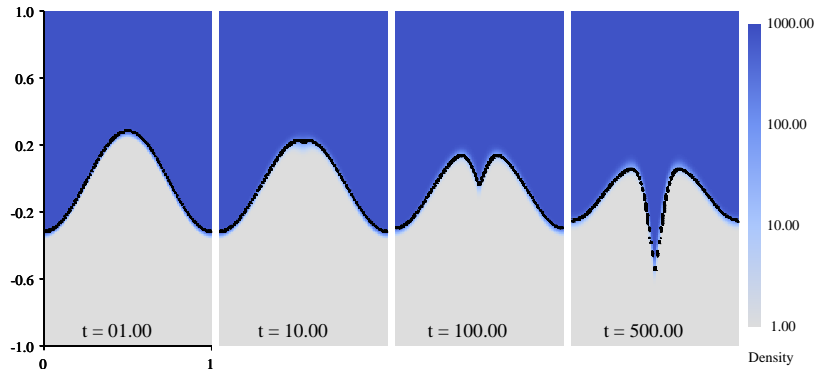
A high-order accurate computational solution strategy is invoked

- An in-house developed code is used to solve the Euler equations.
- Numerical methods
 - 3rd order Discontinuous Galerkin method is used in space
 - 4th order Runge-Kutta time marching
 - Roe Solver used to handle discontinuities
- Acoustic waves are prescribed within the domain.
- Grid stretching reduces reflections.
- Grid size: $\lambda \times 70\lambda (L_x \times L_y)$



The theoretical interface dynamics are simulated

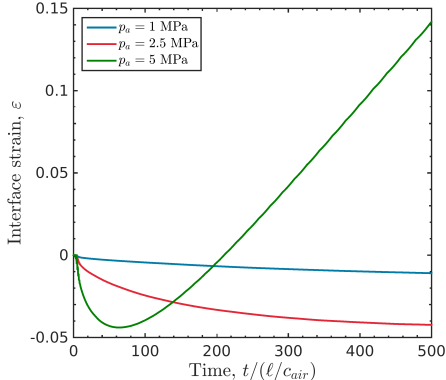
Perturbation and wave amplitudes are varied: $a_0 = 0.03\ell, 0.1\ell, 0.3\ell$;
 $p_a = 1, 2.5, 5 \text{ MPa}$.



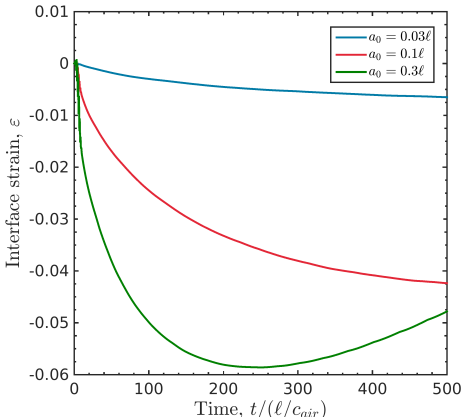
(a) $a_0 = 0.3\ell, p_a = 5 \text{ MPa}$

Figure: The evolution of the interface is shown for $t = 0, 10, 100$, and 500 for varying initial perturbation amplitudes and a wave amplitude of $p_a = 5 \text{ Pa}$.

Interface strains are compared to known failure thresholds



(a) $p_a = 1, 2.5, 5 \text{ MPa}; a_0 = 0.1\ell$



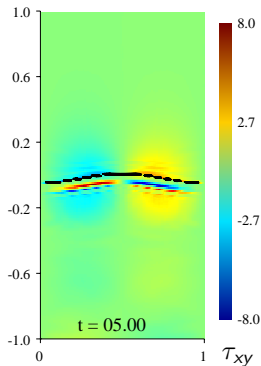
(b) $p_a = 2.5 \text{ MPa}; a_0 = 0.03\ell, 0.1\ell, 0.3\ell$

$$\varepsilon = \frac{s(t) - s_0}{s_0}$$

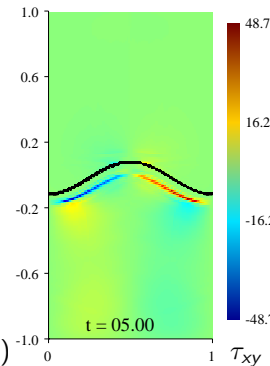
Cyclic strains $\varepsilon \geq 8\%$ have been found to cause consistent failure of alveolar epithelial cells Belete *et al.* (2010).

Theoretical Newtonian viscous stresses are calculated and compared to known stress failure thresholds.

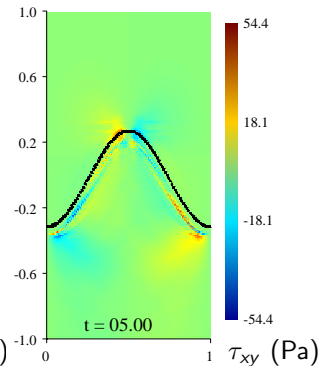
$p_a = 5 \text{ MPa}$ case:



(a) $a_0 = 0.03\ell$



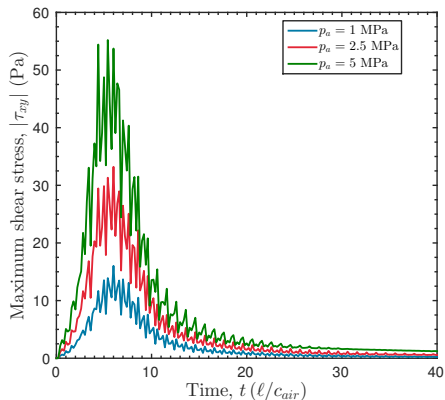
(b) $a_0 = 0.1\ell$



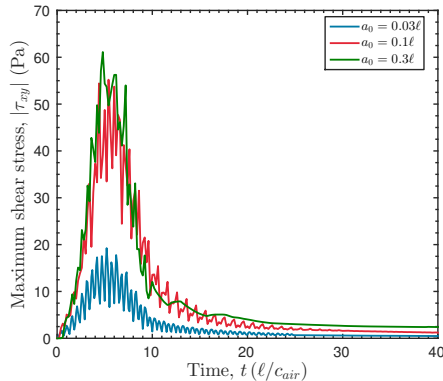
(c) $a_0 = 0.3\ell$

$$\tau_{xy}(x, y, t) = \mu \left(\frac{du}{dy} + \frac{dv}{dx} \right), \quad \mu = \alpha \mu_{\text{water}} + (1 - \alpha) \mu_{\text{air}}$$

Theoretical Newtonian viscous stresses are calculated and compared to known stress failure thresholds.



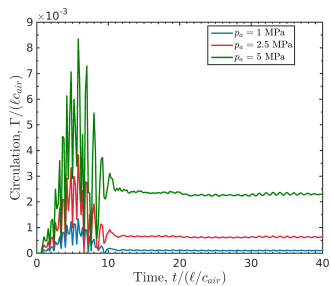
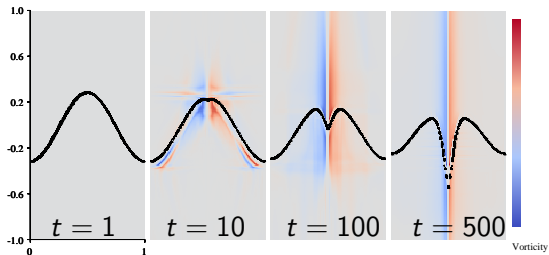
(a) $p_a = 1, 2.5, 5 \text{ MPa}; a_0 = 0.1\ell$



(b) $p_a = 5 \text{ MPa}; a_0 = 0.03\ell, 0.1\ell, 0.3\ell$

- Alveolar failures have been observed to occur for transmural stresses $\geq 3.2 \text{ kPa}$ (West *et al.*, 1991).
- Stresses observed here are far below this failure criterion.

Baroclinic vorticity appears to cause the interface deformation after the wave has passed



- Circulation appears to be the only mechanism remaining to drive the interface motion after the wave passes.
- The amount of circulation deposited increases with wave amplitude.
- This looks similar to Richtmyer-Meshkov / Rayleigh-Taylor instabilities.

Summary and conclusions thus far

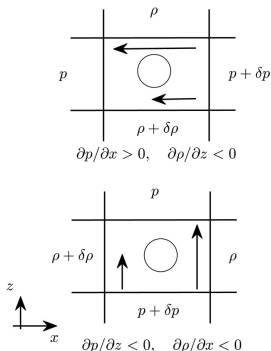
Summary:

- I studied the interaction of ultrasound pulses with gas-liquid interfaces similar to those in the alveoli.

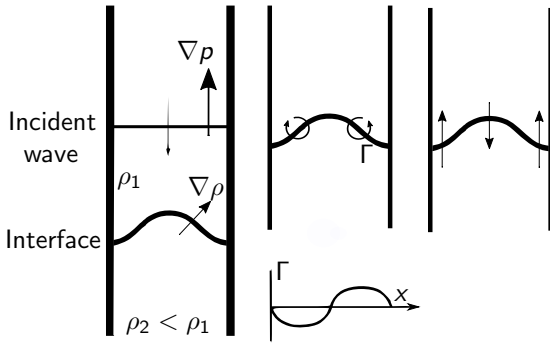
Conclusions

- A single ultrasound pulse may be capable of appreciably deforming an alveolar wall before a subsequent pulse occurs.
- Viscous shear stresses generated by ultrasound are unlikely to be the cause of alveolar hemorrhage.
- Vorticity-induced strain may be capable of causing pulmonary hemorrhage, though more work that accounts for viscoelastic effects and multiple pulses is required.

Shock-driven fluid-fluid interfaces have been studied extensively



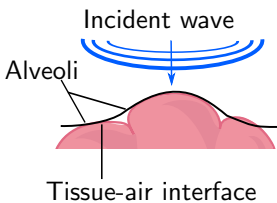
Adapted from Heifetz & Mak (2015)



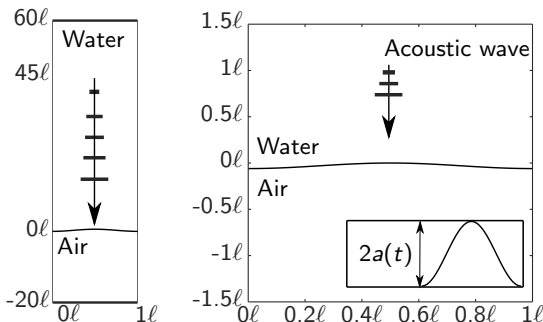
Adapted from Brouillette (2002)

- Shocks deposit baroclinic vorticity at perturbed fluid-fluid interfaces (Drake, 2006).
- This vorticity drives the interface perturbation to grow.
- This is the Richtmyer-Meshkov “instability”.
- Acoustic waves are different. They interact over a finite time-scale.

A model was developed to study acoustically-driven gas-liquid interfaces

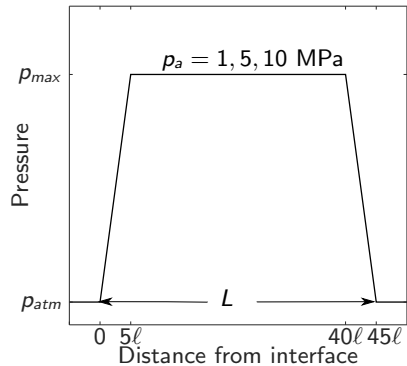
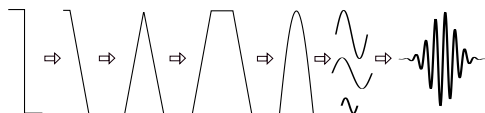


(a) Physical problem schematic



(b) Domain and model problem schematic.

A model was developed to study acoustically-driven gas-liquid interfaces

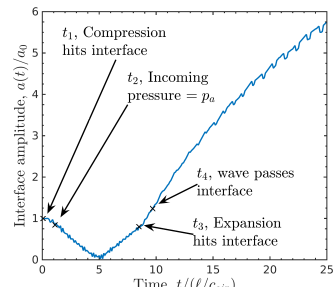
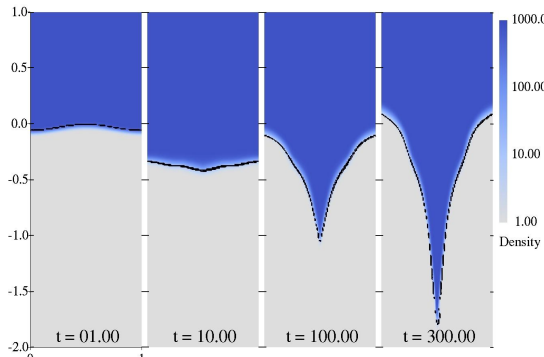


(a) Design of the trapezoidal waveform

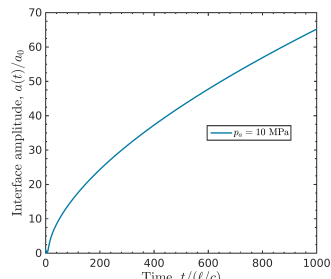
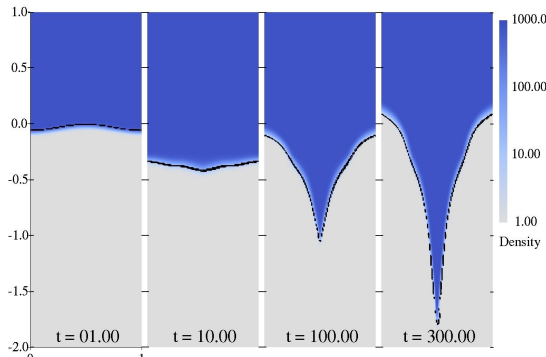
(b) Acoustic pressure waveform

A trapezoidal wave is used to capture features of both the ultrasound pulse and the shock wave, which has been previously studied as the Richtmyer-Meshkov instability.

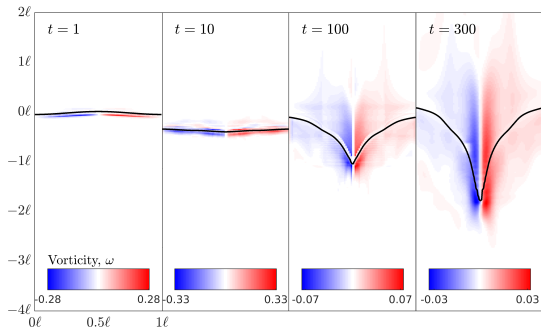
The theoretical dynamics of the interface are calculated for waves of varying amplitude $p_a = 5, 7.5, 10$, and 12.5 MPa.



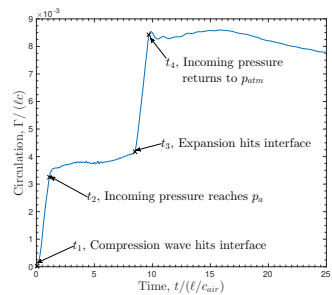
The theoretical dynamics of the interface are calculated for waves of varying amplitude $p_a = 5, 7.5, 10$, and 12.5 MPa.



It is shown that baroclinic vorticity is capable of deforming the interface long after the wave has passed.

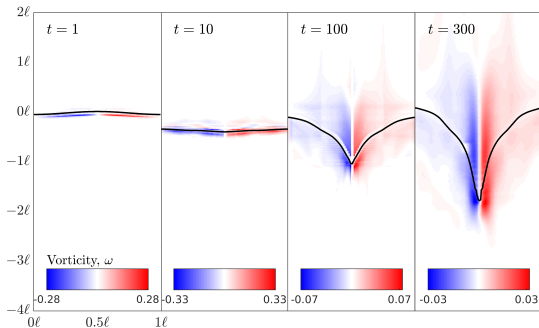


(a) $p_a = 10 \text{ MPa}$.

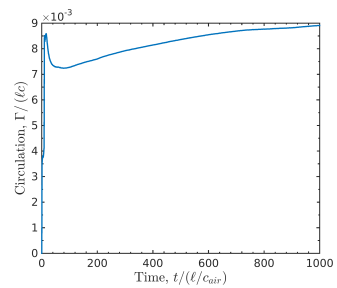


(b) $0 \leq t \leq 25$.

It is shown that baroclinic vorticity is capable of deforming the interface long after the wave has passed.

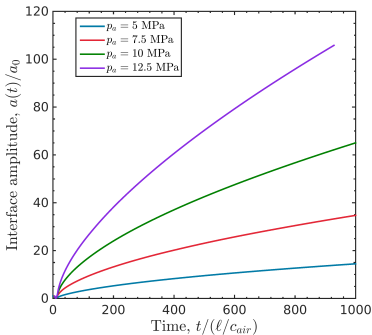


(a) $p_a = 10 \text{ MPa}$.

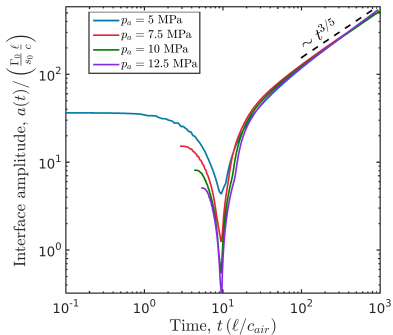


(b) $0 \leq t \leq 1000$.

The interface perturbation amplitude grows approximately as $t^{3/5}$ and scales with the linear circulation density Γ_0/s_0 .

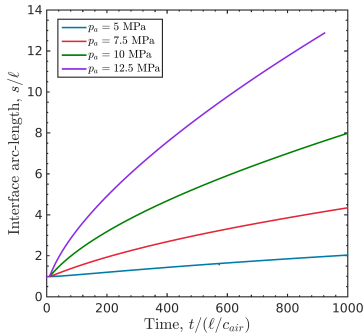


(a) Constant scaling: $a(t)/a_0$

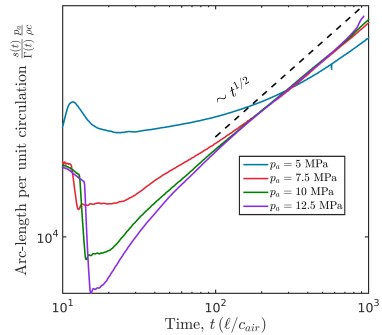


(b) Vortex strength scaling:
 $a(t)/\left(\frac{\Gamma_0 \ell}{s_0 c}\right)$

The interface arc length per unit circulation $s(t)/\Gamma(t)$ grows approximately as $t^{1/2}$ and scales with wave amplitude p_a .

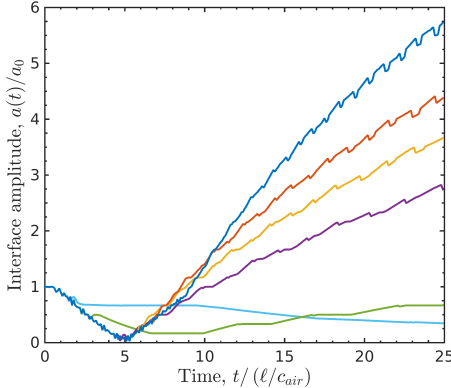


(a) Constant scaling: $s(t)/\ell$

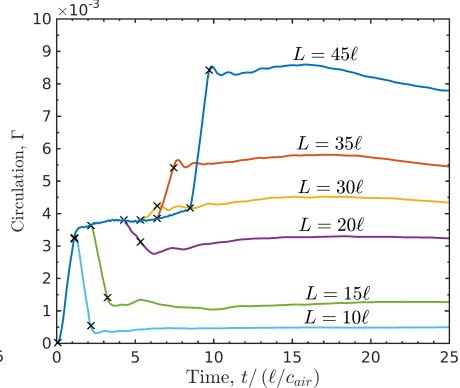


(b) Vortex strength scaling: $\frac{s(t)}{\Gamma(t)} \frac{p_a}{\rho c}$

The circulation deposited and therefore late time perturbation growth depend heavily on time-dependent wave features



(a) $a(t)/a_0$



(b) $\Gamma(t)$

The interface amplitude (left) and circulation (right) histories for waves of varying total length L and elevated static pressure duration between the expansion and compression. Here we show results for $L = 45\ell$ (blue), $L = 35\ell$ (orange), $L = 30\ell$ (yellow), $L = 20\ell$ (purple), $L = 15\ell$ (green), $L = 10\ell$ (light blue)

Summary and conclusions thus far

Summary:

- I studied the interaction of finite-duration acoustic waves with gas-liquid interfaces.

Conclusions

- Acoustically generated baroclinic vorticity generated by wave-interface interaction is capable of deforming perturbed liquid-gas interfaces.
- The interface perturbation grows as $t^{3/5}$ and scales with linear circulation density along the interface Γ_0/s_0 .
- The interface arc length per unit circulation $s(t)/\Gamma(t)$ grows approximately as $t^{1/2}$ and scales with wave amplitude p_a .
- Circulation deposition depends on interface morphology and time-dependent wave features.

Part II: Area statistics

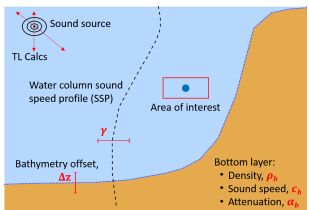
Past work: Efficient estimation of the probability density function of transmission loss in uncertain ocean environments

Transmission Loss, $TL = 20 \log_{10} \left(\frac{P_{source}}{P_{receiver}} \right)$, is useful for naval applications.

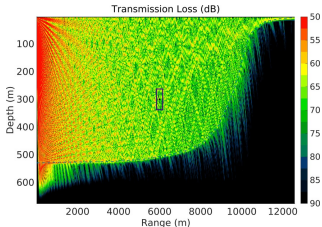
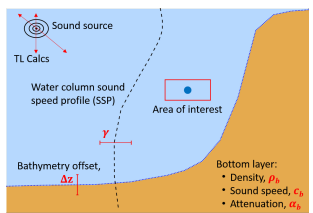


TL uncertainty is important for those making decisions based on TL, but traditional methods are slow and expensive.

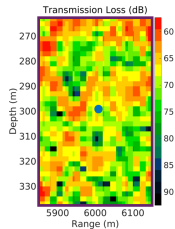
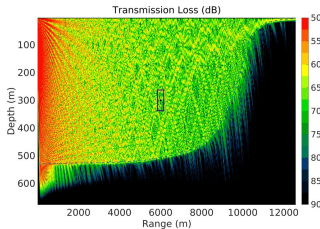
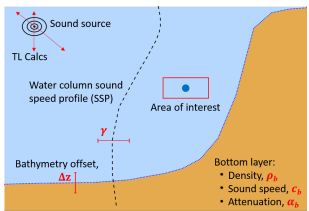
Past work: We developed a computationally efficient way of computing TL in uncertain environments



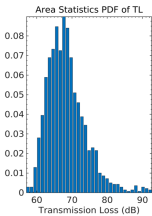
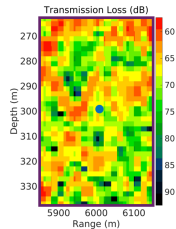
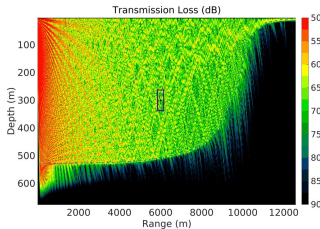
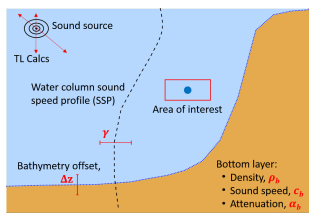
Past work: We developed a computationally efficient way of computing TL in uncertain environments



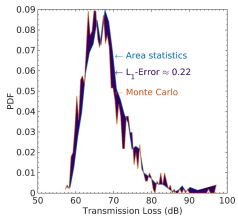
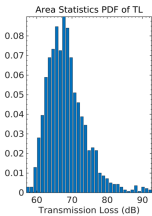
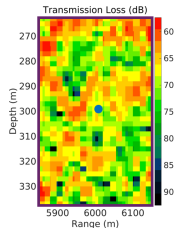
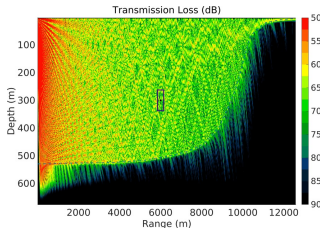
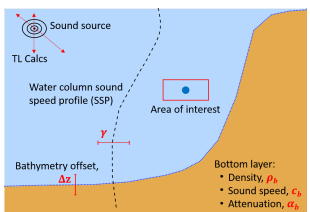
Past work: We developed a computationally efficient way of computing TL in uncertain environments



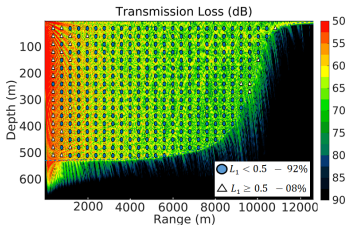
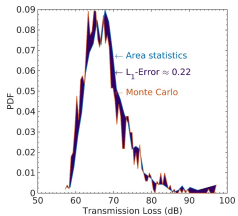
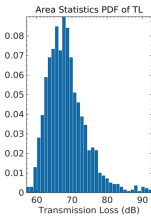
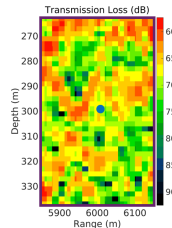
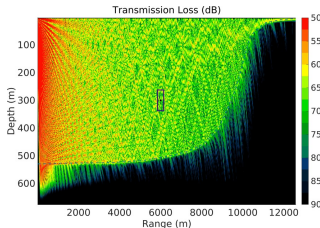
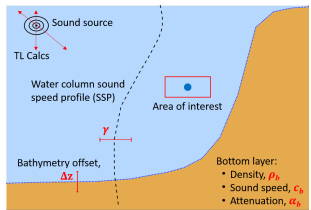
Past work: We developed a computationally efficient way of computing TL in uncertain environments



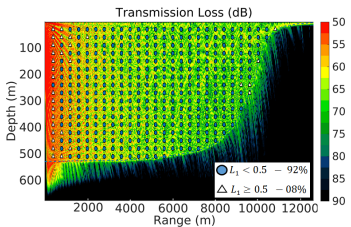
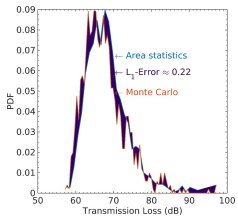
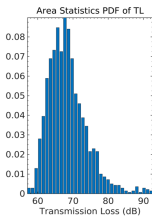
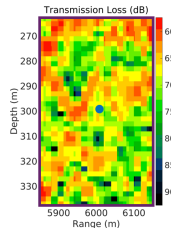
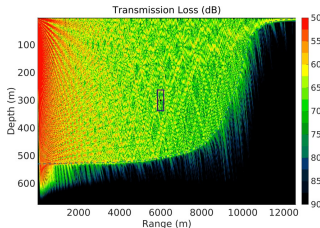
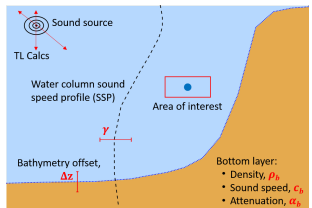
Past work: We developed a computationally efficient way of computing TL in uncertain environments



Past work: We developed a computationally efficient way of computing TL in uncertain environments



Past work: We developed a computationally efficient way of computing TL in uncertain environments



- Engineering level accurate (L_1 -error < 0.5) in 93% of test cases in bottom reflecting environments.
- $\approx \mathcal{O}(10^{-6})$ the cost of 1000-sample Monte Carlo Methods.

EXTRA SLIDES

Past work: Theoretical microbubble dynamics in a viscoelastic medium at capillary breaching thresholds



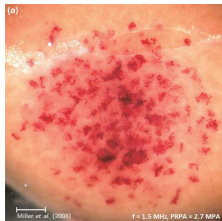
Patterson, B., Miller, D. L., & Johnsen, E. (2012). Theoretical microbubble dynamics in a viscoelastic medium at capillary breaching thresholds. JASA, 132(6), 3770.

Past work: Theoretical microbubble dynamics in a viscoelastic medium at capillary breaching thresholds



$$\left(1 - \frac{\dot{R}}{C}\right) R \ddot{R} + \frac{3}{2} \left(1 - \frac{\dot{R}}{3C}\right) \dot{R}^2 = \left(1 + \frac{\dot{R}}{C}\right) \left[p_B - 1 - p_a - \frac{R}{C} \frac{dp_a}{dt}\right] + \frac{R}{C} \dot{p}_B,$$
$$p_B = \left(1 + \frac{2}{We}\right) \frac{1}{R^{3\gamma}} - \frac{2}{WeR} + \tau_R,$$

Past work: Theoretical microbubble dynamics in a viscoelastic medium at capillary breaching thresholds



$$\left(1 - \frac{\dot{R}}{C}\right) R \ddot{R} + \frac{3}{2} \left(1 - \frac{\dot{R}}{3C}\right) \dot{R}^2 = \left(1 + \frac{\dot{R}}{C}\right) \left[p_B - 1 - p_a - \frac{R}{C} \frac{dp_a}{dt}\right] + \frac{R}{C} \dot{p}_B,$$
$$p_B = \left(1 + \frac{2}{We}\right) \frac{1}{R^{3\gamma}} - \frac{2}{WeR} + \tau_R,$$

Parameter	Dimensional value	Dimensionless number
Viscosity	$\mu = 0.015 \text{ (Pa s)}$	$\Rightarrow Re = \rho u R_o / \mu = 2/3$
Elasticity	$G = 10^5 \text{ (Pa)}$	$\Rightarrow Ca = \rho u^2 / G = 1.0$
Surface tension	$S = 0.056 \text{ (N/m)}$	$\Rightarrow We = \rho u^2 R_o / S = 2$
Sound speed	$c = 1570 \text{ (m/s)}$	$\Rightarrow C = c/u = 157$

Patterson, B., Miller, D. L., & Johnsen, E. (2012). Theoretical microbubble dynamics in a viscoelastic medium at capillary breaching thresholds. JASA, 132(6), 3770.

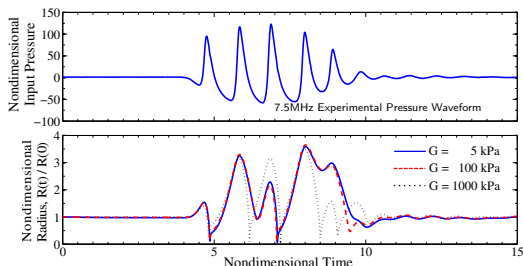
Past work: Theoretical microbubble dynamics in a viscoelastic medium at capillary breaching thresholds



$$\left(1 - \frac{\dot{R}}{C}\right) R \ddot{R} + \frac{3}{2} \left(1 - \frac{\dot{R}}{3C}\right) \dot{R}^2 = \left(1 + \frac{\dot{R}}{C}\right) \left[p_B - 1 - p_a - \frac{R}{C} \frac{dp_a}{dt}\right] + \frac{R}{C} \dot{p}_B,$$

$$p_B = \left(1 + \frac{2}{We}\right) \frac{1}{R^{3\gamma}} - \frac{2}{WeR} + \tau_R,$$

Parameter	Dimensional value	Dimensionless number
Viscosity	$\mu = 0.015 \text{ (Pa s)}$	$\rightarrow Re = \rho u R_o / \mu = 2/3$
Elasticity	$G = 10^5 \text{ (Pa)}$	$\rightarrow Ca = \rho u^2 / G = 1.0$
Surface tension	$S = 0.056 \text{ (N/m)}$	$\rightarrow We = \rho u^2 R_o / S = 2$
Sound speed	$c = 1570 \text{ (m/s)}$	$\rightarrow C = c/u = 157$



Patterson, B., Miller, D. L., & Johnsen, E. (2012). Theoretical microbubble dynamics in a viscoelastic medium at capillary breaching thresholds. JASA, 132(6), 3770.

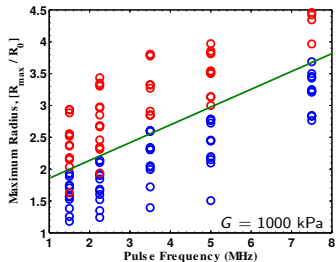
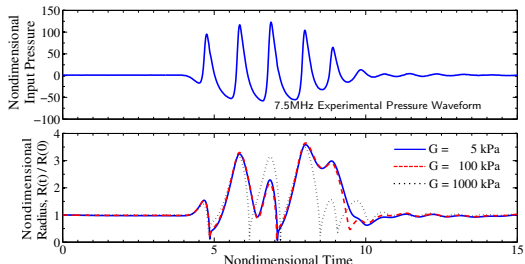
Past work: Theoretical microbubble dynamics in a viscoelastic medium at capillary breaching thresholds



$$\left(1 - \frac{\dot{R}}{C}\right) R \ddot{R} + \frac{3}{2} \left(1 - \frac{\dot{R}}{3C}\right) \dot{R}^2 = \left(1 + \frac{\dot{R}}{C}\right) \left[p_B - 1 - p_a - \frac{R}{C} \frac{dp_a}{dt}\right] + \frac{R}{C} \dot{p}_B,$$

$$p_B = \left(1 + \frac{2}{We}\right) \frac{1}{R^{3\gamma}} - \frac{2}{WeR} + \tau_R,$$

Parameter	Dimensional value	Dimensionless number
Viscosity	$\mu = 0.015 \text{ (Pa s)}$	$\rightarrow Re = \rho u R_o / \mu = 2/3$
Elasticity	$G = 10^5 \text{ (Pa)}$	$\rightarrow Ca = \rho u^2 / G = 1.0$
Surface tension	$S = 0.056 \text{ (N/m)}$	$\rightarrow We = \rho u^2 R_o / S = 2$
Sound speed	$c = 1570 \text{ (m/s)}$	$\rightarrow C = c/u = 157$

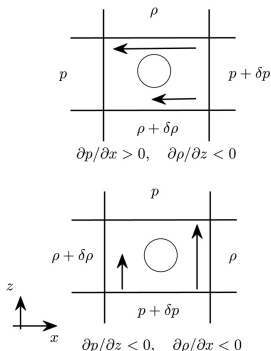


Patterson, B., Miller, D. L., & Johnsen, E. (2012). Theoretical microbubble dynamics in a viscoelastic medium at capillary breaching thresholds. JASA, 132(6), 3770.

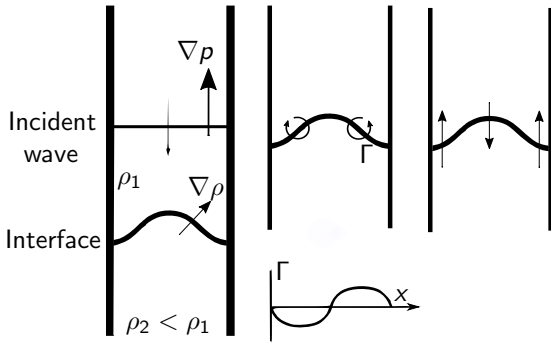
Part II: Current Project

Diagnostic ultrasound-induced lung hemorrhage and acoustic wave interactions with liquid-gas interfaces

Shock-driven fluid-fluid interfaces have been studied extensively



Adapted from Heifetz & Mak (2015)



Adapted from Brouillette (2002)

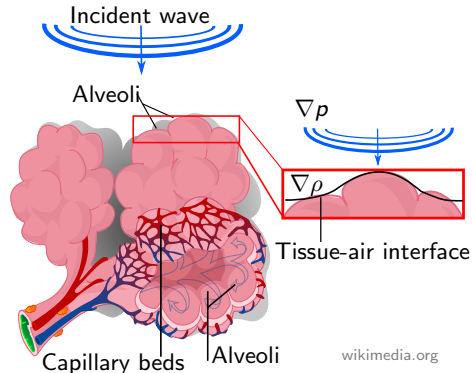
- Shocks deposit baroclinic vorticity at perturbed fluid-fluid interfaces (Drake, 2006).
- This vorticity drives the interface perturbation to grow.
- This is the Richtmyer-Meshkov “instability”.
- Acoustic waves are different. They interact over a finite time-scale.

We aim to use fluid mechanics with computational modeling and simulations to investigate the underlying physics of DUS-lung interaction:

Acoustic wave interactions with liquid-gas interfaces.

We hypothesize that US waves generate baroclinic vorticity at air-tissue interfaces in the lungs, straining fragile alveolar walls.

- Alveolar air-tissue interfaces have sharp density gradients
- US has strong pressure gradients
- US-induced baroclinic vorticity may cause strain, similar to shock-driven interfaces
- Linear acoustics does not capture this.

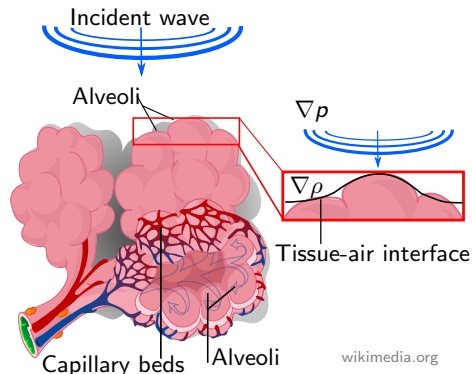


We hypothesize that US waves generate baroclinic vorticity at air-tissue interfaces in the lungs, straining fragile alveolar walls.

The vorticity generation equation

$$\frac{\partial \omega}{\partial t} + (\mathbf{u} \cdot \nabla) \omega = (\omega \cdot \nabla) \mathbf{u} - \omega (\nabla \cdot \mathbf{u}) + \frac{\nabla \rho \times \nabla p}{\rho^2} - \nabla \times \left(\frac{\nabla \cdot \boldsymbol{\tau}}{\rho} \right) + \nabla \times \mathbf{B}$$

- Alveolar air-tissue interfaces have sharp density gradients
- US has strong pressure gradients
- US-induced baroclinic vorticity may cause strain, similar to shock-driven interfaces
- Linear acoustics does not capture this.



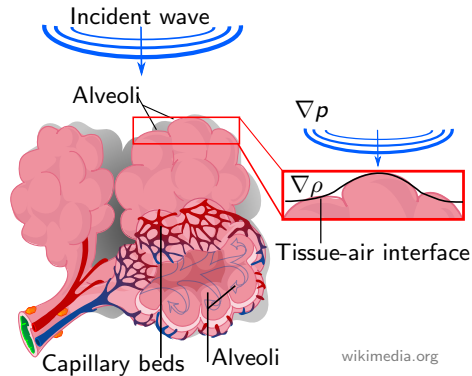
wikimedia.org

We hypothesize that US waves generate baroclinic vorticity at air-tissue interfaces in the lungs, straining fragile alveolar walls.

The vorticity generation equation

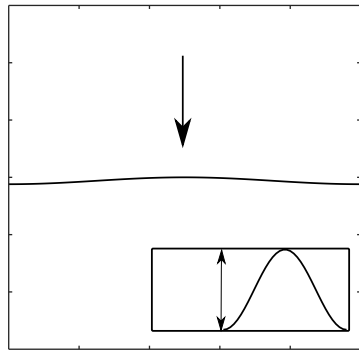
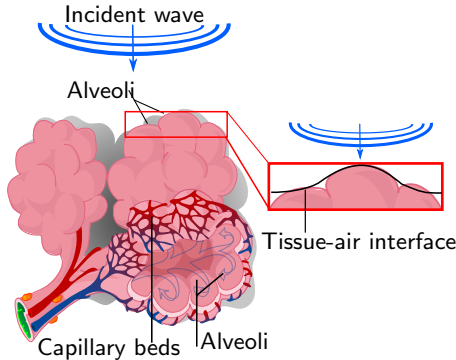
$$\frac{\partial \omega}{\partial t} + (\mathbf{u} \cdot \nabla) \omega = (\omega \cdot \nabla) \mathbf{u}^0 - \omega (\nabla \cdot \mathbf{u}) + \frac{\nabla p \times \nabla p}{\rho^2} - \nabla \times \left(\frac{\nabla p}{\rho} \right)^0 + \nabla \times \mathbf{B}^0$$

- Alveolar air-tissue interfaces have sharp density gradients
- US has strong pressure gradients
- US-induced baroclinic vorticity may cause strain, similar to shock-driven interfaces
- Linear acoustics does not capture this.



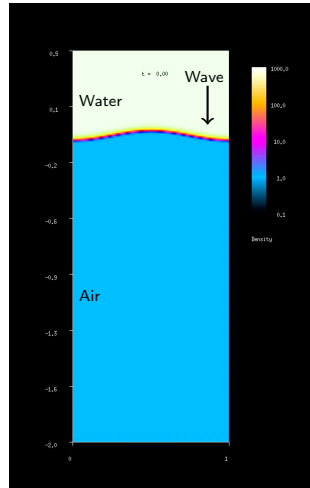
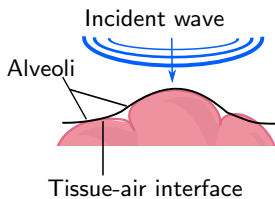
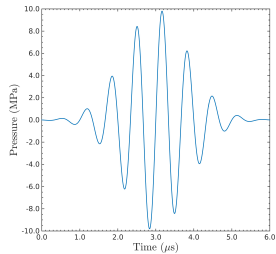
wikimedia.org

Problem setup: We model the ultrasound-alveolar interaction as a 2D, compressible, inviscid fluid system.

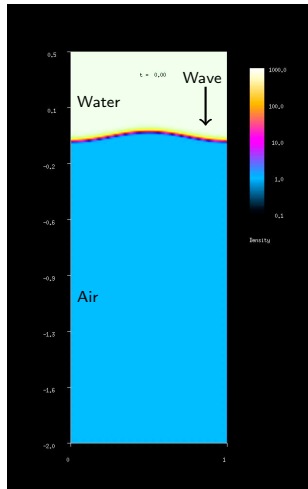
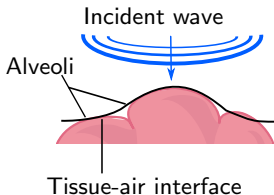
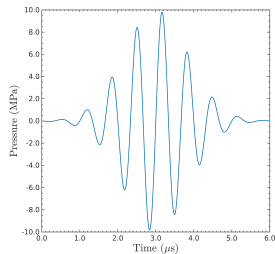


An acoustic wave impinges downward from water toward a perturbed air interface ($a_0=0.06\lambda$).

We simulated and US-pulse impinging on a water-air interface

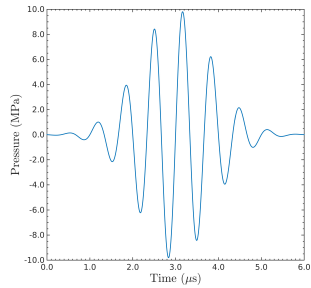


We simulated and US-pulse impinging on a water-air interface

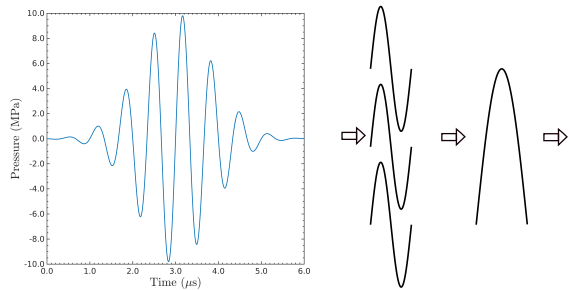


- Linear acoustics doesn't explain the interface deformation.
- The DUS pulse is complicated and not ideal for analysis.

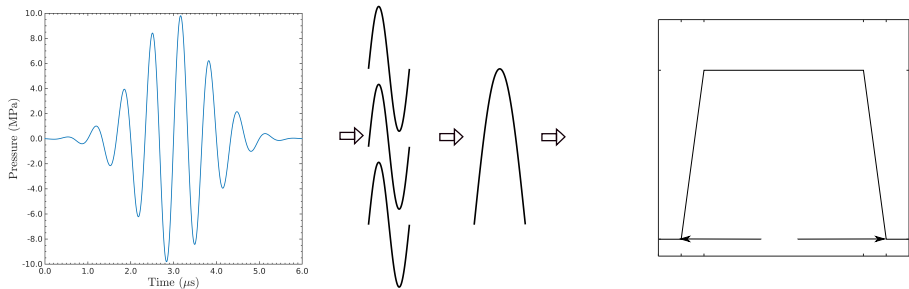
US pulse and Trapezoidal acoustic waveforms are used.



US pulse and Trapezoidal acoustic waveforms are used.



US pulse and Trapezoidal acoustic waveforms are used.



- The trapezoidal waves is simple for understanding physics and analysis, but able to capture feature of US pulse.
- Pulse waveforms are used to check relevance to DUS.

Governing Equations

Euler equations of fluid motion

$$\frac{\partial \rho}{\partial t} + \frac{\partial (\rho u)}{\partial x} + \frac{\partial (\rho v)}{\partial y} = 0,$$

$$\frac{\partial \rho u}{\partial t} + \frac{\partial}{\partial x} \left(\rho u^2 + p \right) + \frac{\partial}{\partial y} (\rho uv) = 0,$$

$$\frac{\partial \rho v}{\partial t} + \frac{\partial}{\partial x} (\rho uv) + \frac{\partial}{\partial y} \left(\rho v^2 + p \right) = 0,$$

$$\frac{\partial E}{\partial t} + \frac{\partial}{\partial x} [u(E + p)] + \frac{\partial}{\partial y} [v(E + p)] = 0,$$

Stiffened equation of state

$$E = \frac{\rho(u^2 + v^2)}{2} + \frac{p + \gamma B}{\gamma - 1}.$$

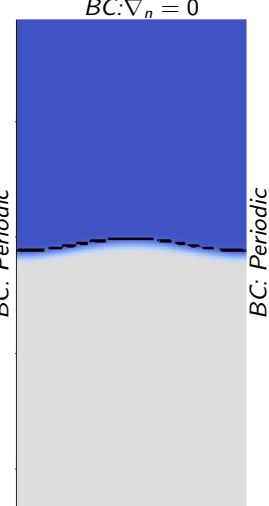
Advection equations for γ, B prevent interface pressure oscillations.

$$\frac{\partial}{\partial t} \left(\frac{\gamma B}{\gamma - 1} \right) + u \frac{\partial}{\partial x} \left(\frac{\gamma B}{\gamma - 1} \right) + v \frac{\partial}{\partial y} \left(\frac{\gamma B}{\gamma - 1} \right) = 0,$$

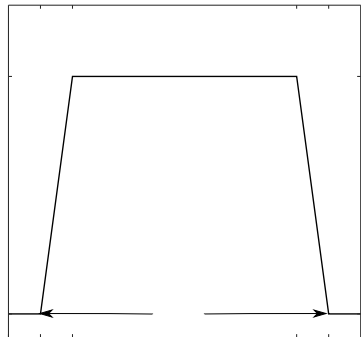
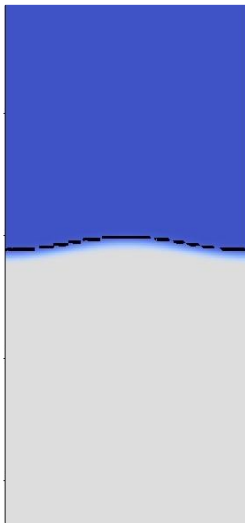
$$\frac{\partial}{\partial t} \left(\frac{1}{\gamma - 1} \right) + u \frac{\partial}{\partial x} \left(\frac{1}{\gamma - 1} \right) + v \frac{\partial}{\partial y} \left(\frac{1}{\gamma - 1} \right) = 0$$

A high-order accurate computational solution strategy is invoked

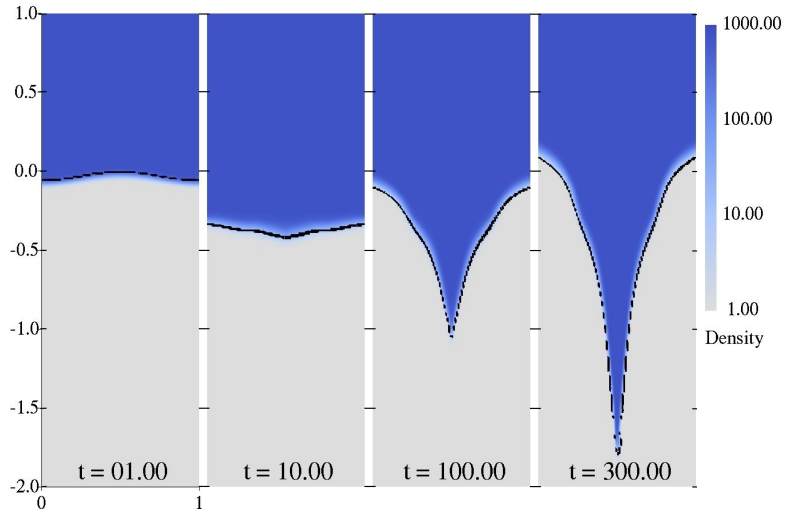
- An in-house developed code is used to solve the Euler equations.
- Numerical methods
 - 3rd order Discontinuous Galerkin method is used in space
 - 4th order Runge-Kutta time marching
 - Roe Solver used to handle discontinuities
- Acoustic waves are prescribed within the domain.
- Grid stretching reduces reflections.
- Grid size: $\lambda \times 70\lambda (L_x \times L_y)$



Base case: a 10 MPa trapezoidal wave hits the sinusoidal interface

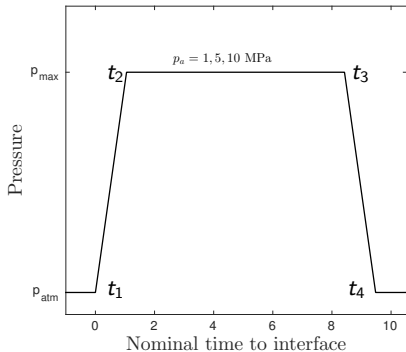
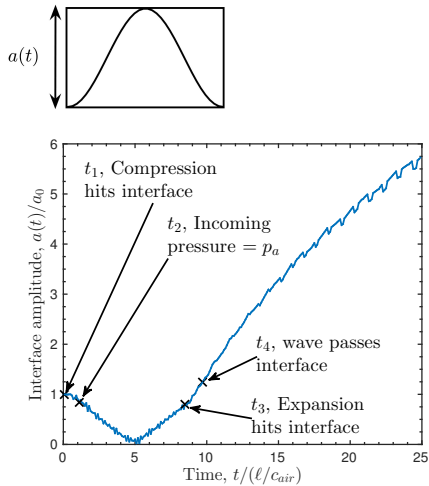


Results: Evolution of the interface after 10 MPa trapezoidal wave



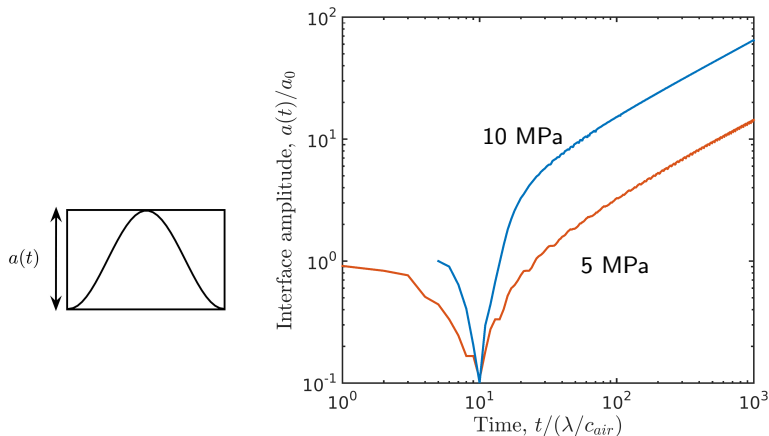
The interface perturbation evolves from a smooth sinusoid into a sharp point.

Results: Early evolution of the interface



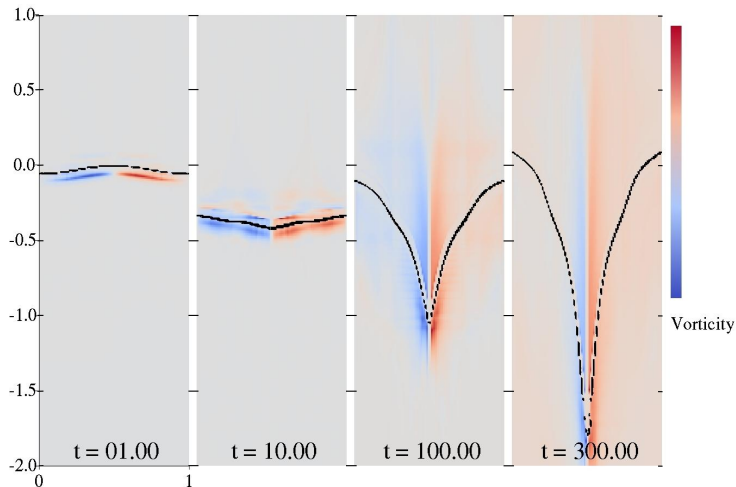
The interface perturbation is initially compressed ($0^+ \leq t \leq 5$), experiences a phase change ($t = 5$), then grows $t > 5$.

Results: Late-time evolution of the interface



We suspect vorticity is driving this late time growth.

Results: Vorticity dynamics for the 10 MPa trapezoidal wave

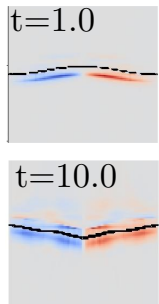
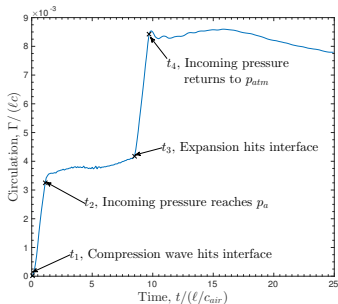
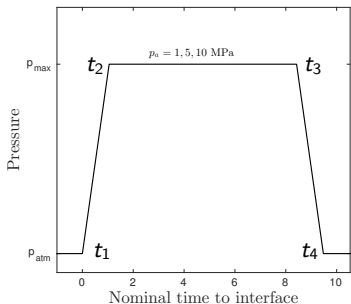


- Vorticity initially deposits in air-dominated ($y_0 < 0.5$) fluid of the interface.
- As the interface evolves, some vorticity advects with it.

Results: A closer look at how circulation is deposited.

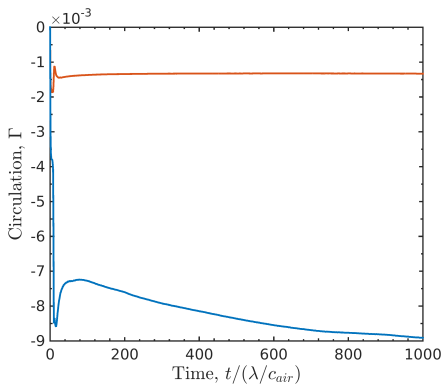
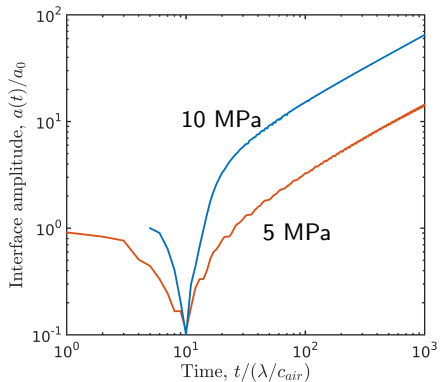
Circulation,

$$\Gamma = \int_{-\infty}^{+\infty} \int_{0.5\lambda}^{1\lambda} \omega \, dx \, dy$$



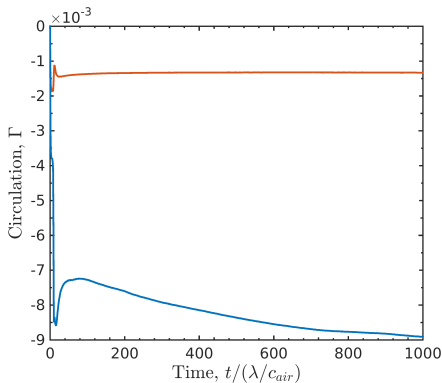
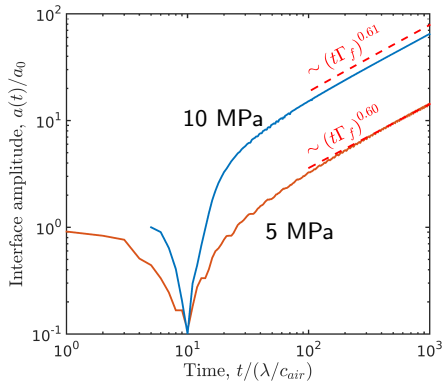
- Both the compression and expansion deposit vorticity.

Results: Late-time evolution of the interface



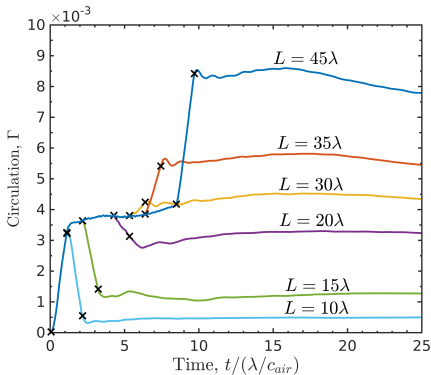
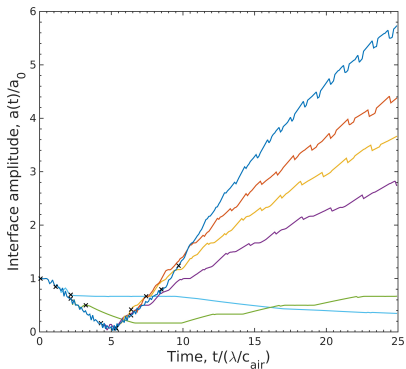
From dimensional analysis, we expect a purely circulation growth of the interface perturbation to behave according to $a(t) \sim \sqrt{\Gamma t}$.

Results: Late-time evolution of the interface



From dimensional analysis, we expect a purely circulation growth of the interface perturbation to behave according to $a(t) \sim \sqrt{\Gamma t}$.

Results: Dependence of interface dynamics on wave duration



- Changing wave width changes time when expansion hits interface.
- Time-dependent interface deformation causes time-dependent vorticity deposition.
- The long-term interface dynamics can change appreciably.

Order of magnitude analysis of vorticity generation

$$\frac{\partial \vec{\omega}}{\partial t} + (\vec{u} \cdot \nabla) \vec{\omega} = -\vec{\omega} (\nabla \cdot \vec{u}) + \frac{\nabla \rho \times \nabla p}{\rho^2}.$$

Order of magnitude analysis of vorticity generation

$$\frac{\partial \vec{\omega}}{\partial t} + (\vec{u} \cdot \nabla) \vec{\omega} = -\vec{\omega} (\nabla \cdot \vec{u}) + \frac{\nabla \rho \times \nabla p}{\rho^2}.$$

Acoustic Relations and operator treatments

$$\Delta p_a = \pm \Delta u_a \rho c = c^2 \Delta \rho_a, \quad \|\nabla f\| \sim \|\nabla \cdot f\| \sim \|\nabla \times f\| = \mathcal{O}(|\Delta f| / \Delta L)$$

Order of magnitude analysis of vorticity generation

$$\frac{\partial \vec{\omega}}{\partial t} + (\vec{u} \cdot \nabla) \vec{\omega} = -\vec{\omega} (\nabla \cdot \vec{u}) + \frac{\nabla \rho \times \nabla p}{\rho^2}.$$

Acoustic Relations and operator treatments

$$\Delta p_a = \pm \Delta u_a \rho c = c^2 \Delta \rho_a, \quad \|\nabla f\| \sim \|\nabla \cdot f\| \sim \|\nabla \times f\| = \mathcal{O}(|\Delta f| / \Delta L)$$

Baroclinic vorticity generation

$$\left\| \frac{\nabla \rho \times \nabla p}{\rho^2} \right\| = \mathcal{O} \left(\frac{|\Delta \rho_I| |\Delta p_a|}{|\Delta L_I| |\Delta L_a|} \frac{1}{|\rho|^2} |\theta| \right)$$

Order of magnitude analysis of vorticity generation

$$\frac{\partial \vec{\omega}}{\partial t} + (\vec{u} \cdot \nabla) \vec{\omega} = -\vec{\omega} (\nabla \cdot \vec{u}) + \frac{\nabla \rho \times \nabla p}{\rho^2}.$$

Acoustic Relations and operator treatments

$$\Delta p_a = \pm \Delta u_a \rho c = c^2 \Delta \rho_a, \quad \|\nabla f\| \sim \|\nabla \cdot f\| \sim \|\nabla \times f\| = \mathcal{O}(|\Delta f| / \Delta L)$$

Baroclinic vorticity generation

$$\left\| \frac{\nabla \rho \times \nabla p}{\rho^2} \right\| = \mathcal{O} \left(\frac{|\Delta \rho_I| |\Delta p_a|}{|\Delta L_I| |\Delta L_a|} \frac{1}{|\rho|^2} |\theta| \right)$$

Advective and compressible vorticity generation - $\|\vec{\omega}\| = \int_0^{\Delta t_a} (\text{baroclinic term}) dt$

$$\|(\vec{u} \cdot \nabla) \vec{\omega}\| \sim \|-\vec{\omega} (\nabla \cdot \vec{u})\| = \mathcal{O} \left(\left[\frac{|\Delta u_a|}{|\Delta L_a|} \right]^2 \right),$$

Order of magnitude analysis of vorticity generation

$$\frac{\partial \vec{\omega}}{\partial t} + (\vec{u} \cdot \nabla) \vec{\omega} = -\vec{\omega} (\nabla \cdot \vec{u}) + \frac{\nabla \rho \times \nabla p}{\rho^2}.$$

Acoustic Relations and operator treatments

$$\Delta p_a = \pm \Delta u_a \rho c = c^2 \Delta \rho_a, \quad \|\nabla f\| \sim \|\nabla \cdot f\| \sim \|\nabla \times f\| = \mathcal{O}(|\Delta f| / \Delta L)$$

Baroclinic vorticity generation

$$\left\| \frac{\nabla \rho \times \nabla p}{\rho^2} \right\| = \mathcal{O} \left(\frac{|\Delta \rho_I| |\Delta p_a|}{|\Delta L_I| |\Delta L_a|} \frac{1}{|\rho|^2} |\theta| \right)$$

Advective and compressible vorticity generation - $\|\vec{\omega}\| = \int_0^{\Delta t_a} (\text{baroclinic term}) dt$

$$\|(\vec{u} \cdot \nabla) \vec{\omega}\| \sim \|-\vec{\omega} (\nabla \cdot \vec{u})\| = \mathcal{O} \left(\left[\frac{|\Delta u_a|}{|\Delta L_a|} \right]^2 \right),$$

Comparing terms for our problem

$$\Delta t_a \approx 5\lambda/c_w, \quad \Delta L_a = 5\lambda, \quad \Delta p_a = 10 \text{ MPa}, \quad \Delta L_I \approx 0.05\lambda, \quad <|\theta|> = 0.12$$

$$\frac{\left\| \frac{\nabla \rho \times \nabla p}{\rho^2} \right\|}{\|-\vec{\omega} (\nabla \cdot \vec{u})\|} = \frac{c}{|\Delta u_a|} = \frac{\rho}{|\Delta \rho_a|} = \mathcal{O}(10^2)$$

Order of magnitude analysis of vorticity generation

$$\frac{\partial \vec{\omega}}{\partial t} + (\vec{u} \cdot \nabla) \vec{\omega} = -\vec{\omega} (\nabla \cdot \vec{u}) + \frac{\nabla \rho \times \nabla p}{\rho^2}.$$

Acoustic Relations and operator treatments

$$\Delta p_a = \pm \Delta u_a \rho c = c^2 \Delta \rho_a, \quad \|\nabla f\| \sim \|\nabla \cdot f\| \sim \|\nabla \times f\| = \mathcal{O}(|\Delta f| / \Delta L)$$

Baroclinic vorticity generation

$$\left\| \frac{\nabla \rho \times \nabla p}{\rho^2} \right\| = \mathcal{O} \left(\frac{|\Delta \rho_I| |\Delta p_a|}{|\Delta L_I| |\Delta L_a|} \frac{1}{|\rho|^2} |\theta| \right)$$

Advective and compressible vorticity generation - $\|\vec{\omega}\| = \int_0^{\Delta t_a} (\text{baroclinic term}) dt$

$$\|(\vec{u} \cdot \nabla) \vec{\omega}\| \sim \|-\vec{\omega} (\nabla \cdot \vec{u})\| = \mathcal{O} \left(\left[\frac{|\Delta u_a|}{|\Delta L_a|} \right]^2 \right),$$

Comparing terms for our problem

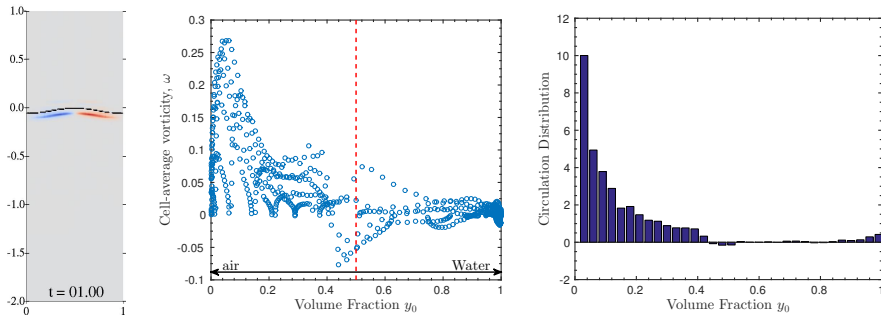
$$\Delta t_a \approx 5\lambda/c_w, \quad \Delta L_a = 5\lambda, \quad \Delta p_a = 10 \text{ MPa}, \quad \Delta L_I \approx 0.05\lambda, \quad <|\theta|> = 0.12$$

$$\frac{\left\| \frac{\nabla \rho \times \nabla p}{\rho^2} \right\|}{\|-\vec{\omega} (\nabla \cdot \vec{u})\|} = \frac{c}{|\Delta u_a|} = \frac{\rho}{|\Delta \rho_a|} = \mathcal{O}(10^2)$$

Calculated values at $t = 1$:

$$\int \frac{\nabla \rho \times \nabla p}{\rho^2} dA = 7.7 \text{e-}3, \quad \int (\vec{u} \cdot \nabla) \vec{\omega} dA = -5.3 \text{e-}5, \quad \int -\vec{\omega} (\nabla \cdot \vec{u}) dA = 2.7 \text{e-}5,$$

Vorticity generation occurs predominately in gas-dominated fluid

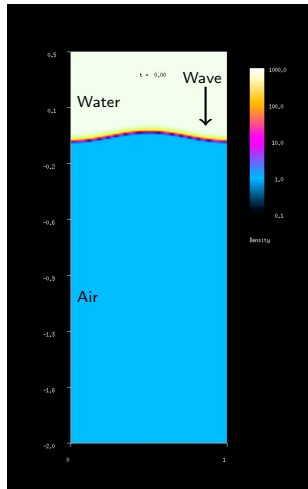
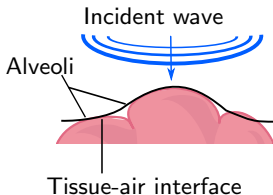
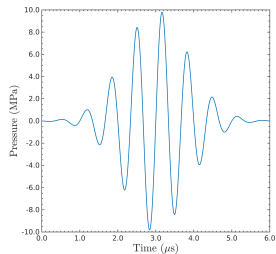


$$\frac{\left\| \frac{\nabla \rho \times \nabla p}{\rho^2} \right\|_{air}}{\left\| \frac{\nabla \rho \times \nabla p}{\rho^2} \right\|_{water}} = \mathcal{O} \left(|\mathbf{T}| \left(\frac{|\rho^-|}{|\rho^+|} \right)^2 \right) \approx 357, \quad (*)$$

$$\mathbf{T} = \frac{2(\rho c)_{air}}{(\rho c)_{air} + (\rho c)_{water}}$$

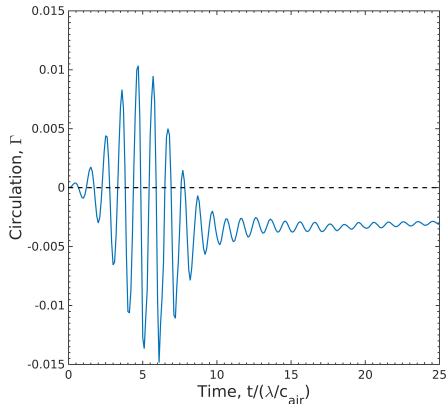
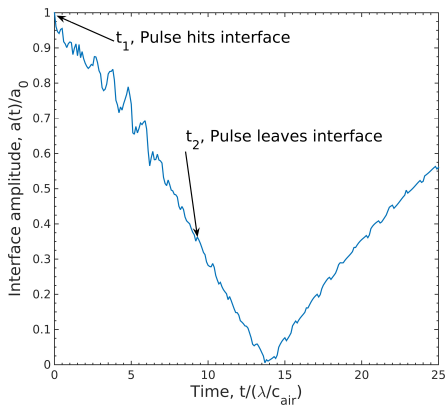
- 97% of circulation appears in fluid with $y_0 < 0.5$
- Computed ratio of circulation in gas-dominated fluid ($y_0 < 0.5$) to liquid-dominated fluid ($y_0 > 0.5$), $\int(*)dA = \mathcal{O}(10^1)$

We simulated and US-pulse impinging on a water-air interface



- Qualitatively this looks like the interface for the trapezoidal wave.
- Longer simulations are needed to check late-time behavior.

Interface response to a 10 MPa US pulse



- Qualitatively, the interface response for the 10 MPa US pulse looks very similar to the 10 MPa trapezoidal wave.
- The circulation deposited is of the same order as the equivalent amplitude trapezoidal wave.

Summary and conclusions thus far

Summary:

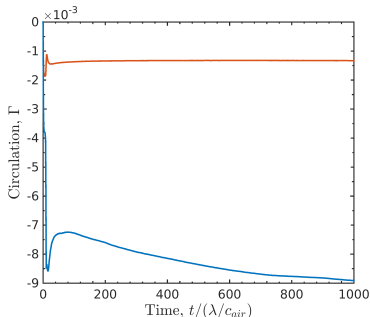
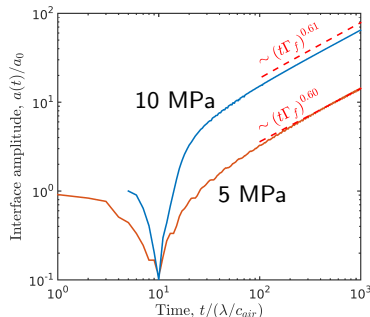
- I studied the interaction of finite-duration acoustic waves with gas-liquid interfaces.

Conclusions

- Baroclinic vorticity generated by wave-interface interaction is likely capable of deforming perturbed liquid-gas interfaces.
- Circulation remaining after the wave determines the long term dynamics.
- Circulation deposition depends on interface morphology.
- Changes in the acoustic waveform that have little affect on the interface during the wave-interface interaction can substantially affect post-wave interface dynamics, via vorticity.
- Baroclinic vorticity is deposited at the interface, predominantly in gas-dominated ($y_0 < 0.5$) fluids.
- Interface responses are qualitatively similar for trapezoidal and US waves.

Part III: Future work

I aim to further our understanding of the relevant fluid mechanics

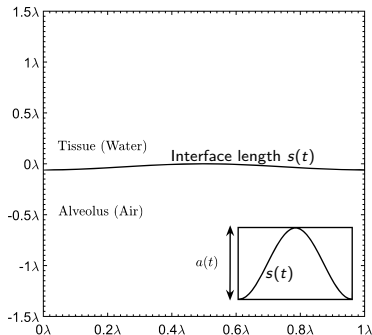


- Explain the discrepancies between numerical results and $a(t) \sim \sqrt{\Gamma t}$
- Develop a model and scaling law for circulation $\Gamma(\nabla p, a_0)$ deposited on a slightly perturbed interface by a compression or expansion wave
- Invert the waves to confirm counter rotating vortices relevant growth

I plan to increase the relevance to DUS

Hypothesis: Baroclinic vorticity drives deformation to the point of stress or strain failure in pulmonary capillaries.

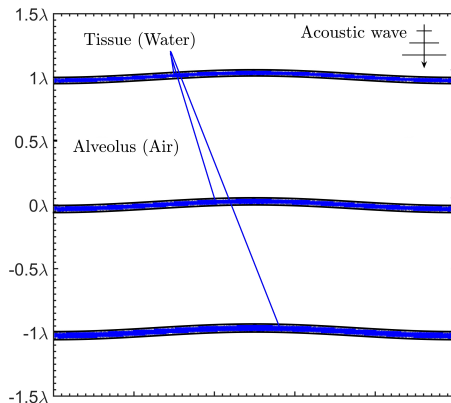
- Rabbit pulmonary capillaries have been shown to hemorrhage at transmural stresses of ≈ 5 kPa (West *et al.*, 1991).
- I will calculate elastic and (passive) viscous stresses at the interface.



I plan to increase the relevance to DUS

Hypothesis: vorticity induced deformation and subsequent hemorrhage will allow acoustic waves and hemorrhage to propagate into subsequent layers of alveoli

- Damage exists in clearly defined hemorrhage area, not behind it (Penney *et al.*, 1993).
- Propagation mechanism of US-induced lesions are unknown (Zachary *et al.*, 2006).



Future work (beyond me)

To fully understand the role that fluid mechanics plays in DUS-induced lung hemorrhage, the following problems need to be addressed:

- Viscous effects
- Elasticity and failure mechanics
- Multiple pulses (via time-dependent boundary conditions)
- Detailed pulmonary structure

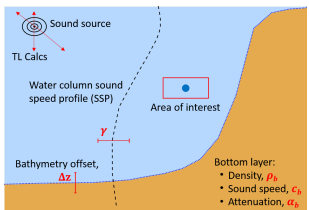
Past work: Efficient estimation of the probability density function of transmission loss in uncertain ocean environments

Transmission Loss, $TL = 20 \log_{10} \left(\frac{P_{source}}{P_{receiver}} \right)$, is useful for naval applications.

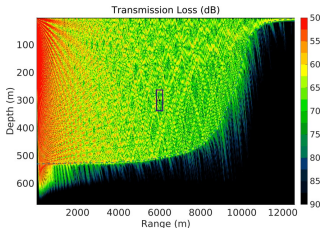
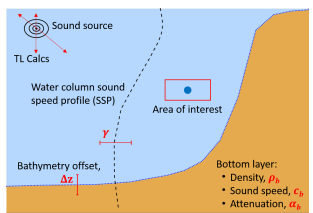


TL uncertainty is important for those making decisions based on TL, but traditional methods are slow and expensive.

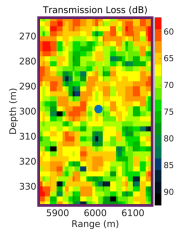
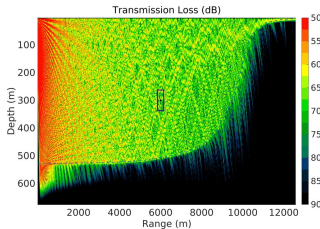
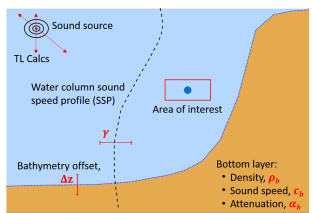
Past work: We developed a computationally efficient way of computing TL in uncertain environments



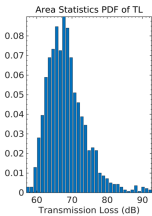
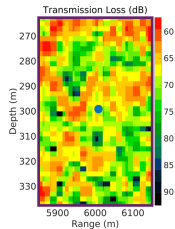
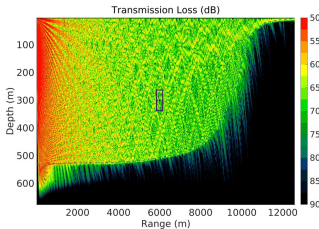
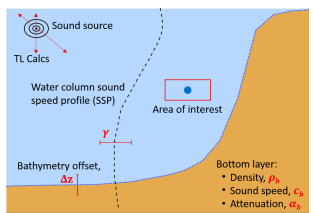
Past work: We developed a computationally efficient way of computing TL in uncertain environments



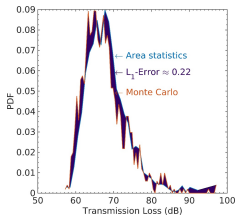
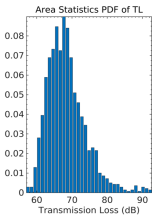
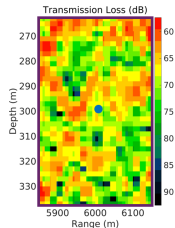
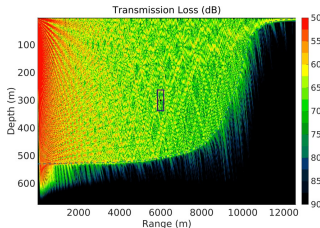
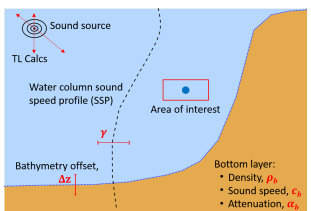
Past work: We developed a computationally efficient way of computing TL in uncertain environments



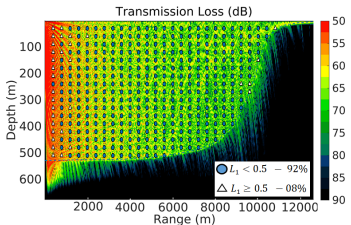
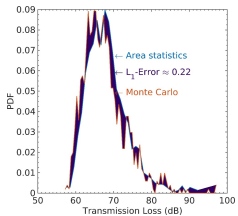
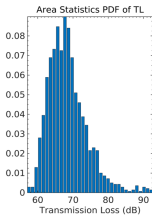
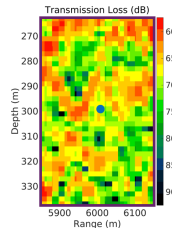
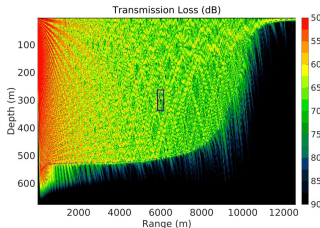
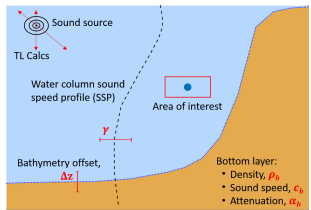
Past work: We developed a computationally efficient way of computing TL in uncertain environments



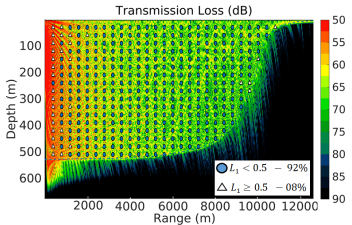
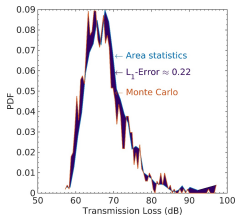
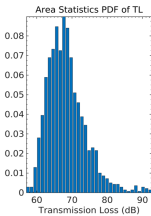
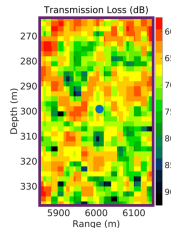
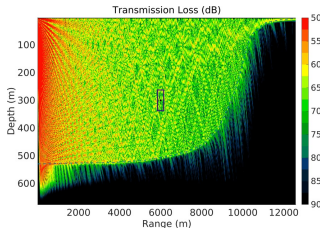
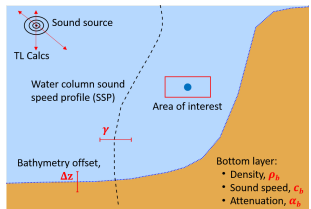
Past work: We developed a computationally efficient way of computing TL in uncertain environments



Past work: We developed a computationally efficient way of computing TL in uncertain environments



Past work: We developed a computationally efficient way of computing TL in uncertain environments



- Engineering level accurate (L_1 -error < 0.5) in 93% of test cases in bottom reflecting environments.
- $\approx \mathcal{O}(10^{-6})$ the cost of 1000-sample Monte Carlo Methods.

Belete, Hewan A, Godin, Lindsay M, Stroetz, Randolph W, & Hubmayr, Rolf D. 2010. Experimental models to study cell wounding and repair. *Cellular physiology and biochemistry : international journal of experimental cellular physiology, biochemistry, and pharmacology*, **25**(1), 71–80.

Beyer, Robert T. 1974. *Nonlinear Acoustics*.

Brouillette, Martin. 2002. The Richtmyer-Meshkov Instability. *Annual review of fluid mechanics*, **34**(1), 445–468.

Child, S.Z., Hartman, C.L., Schery, L.A., & Carstensen, E.L. 1990. Lung damage from exposure to pulsed ultrasound. *Ultrasound in medicine & biology*, **16**(8), 817–825.

Drake, Paul. 2006. *High-Energy-Density Physics*. Shock Wave and High Pressure Phenomena. Springer Berlin Heidelberg.

Heifetz, E., & Mak, J. 2015. Stratified shear flow instabilities in the non-Boussinesq regime. *Physics of fluids*, **27**(8), 086601.

Miller, DL. 2012. Induction of Pulmonary Hemorrhage in Rats During Diagnostic Ultrasound. *Ultrasound in medicine & biology*, **38**(8), 1476–1482.

Miller, Douglas L., Dou, Chunyan, & Wiggins, Roger C. 2008. Frequency Dependence of Kidney Injury Induced by Contrast-Aided Diagnostic Ultrasound in Rats. *Ultrasound in medicine and biology*, **34**(10), 1678–1687.

O'Brien, William D. W.D., & Zachary, J.F. 1997. Lung damage assessment from exposure to pulsed-wave ultrasound in the rabbit, mouse, and pig. *Ieee transactions on ultrasonics, ferroelectrics and frequency control*, **44**(2), 473–485.

Penney, D.P., Schenk, E.A., Maltby, K., Hartman-Raeman, C., Child, S.Z., & Carstensen, E.L. 1993. Morphological effects of pulsed ultrasound in the lung. *Ultrasound in medicine & biology*, **19**(2), 127–135.

Tarantal, Alice F., & Canfield, Don R. 1994. Ultrasound-induced lung hemorrhage in the monkey. *Ultrasound in medicine & biology*, **20**(1), 65–72.

Wei, Kevin, Le, Elizabeth, Bin, Jian-Ping, Coggins, Matthew, Thorpe, Jerrel, & Kaul, Sanjiv. 2001. Quantification of renal blood flow with contrast-enhanced ultrasound. *Journal of the american college of cardiology*, **37**(4), 1135–1140.

West, J B, Tsukimoto, K, Mathieu-Costello, O, & Prediletto, R. 1991.
Stress failure in pulmonary capillaries. *Journal of applied physiology*
(bethesda, md. : 1985), **70**(4), 1731–1742.

Zachary, James F., Blue, James P., Miller, Rita J., Ricconi, Brian J., Eden,
J. Gary, & O'Brien, William D. 2006. Lesions of ultrasound-induced
lung hemorrhage are not consistent with thermal injury. *Ultrasound in
medicine and biology*, **32**(11), 1763–1770.

BACKUP SLIDES

Argument against viscosity - viscous length scales

$$\nu_w = 0.7 \mu\text{m}^2/\text{s}, \quad \nu_a = 16.6 \mu\text{m}^2/\text{s}, \quad f_c = \mathcal{O}(10^6) \text{ Hz}$$

$$\sqrt{\nu_{air}/f_c} = 4\mu \text{ m} = \mathcal{O}(10^{-6}) \ll L_{alveolus} = \mathcal{O}(10^{-4})$$

$$\sqrt{\nu_{air,ND} t} \approx 0.5 < a(t) - a_0 \approx 4 \text{ at } t = 1000$$

Therefore the scale of the viscous effect is smaller than the scale of the problem we are looking at, but may be important at late times.

Dimensional Numbers

- Let $\lambda_{alveolus} = 100\mu \text{ m}$, $u_0 = c_{air} = 343 \text{ m}$, $v_0 = \langle a(t) \rangle \approx 0.65 \text{ m/s}$,
 $u_{intf}(t=20) = 12.8 \text{ m/s}$, $G = 1 \text{ kPa}$
- $\lambda_{alveolus} = 100\mu \text{ m}$, $u_0 = c_{air} = 343 \text{ m}$, $v_0 = \langle a(t) \rangle \approx 0.65 \text{ m/s}$
- $t = 1 \rightarrow t_{dim} = 0.292\mu \text{ s}$

Dimensionless Numbers

- $Fr = \frac{u_0}{\sqrt{g_0 \lambda}} \approx 11000$
- $Fr = \frac{v_0}{\sqrt{g_0 \lambda}} \approx 21$
- $Ca = \frac{\rho u_{intf}^2}{G_{Alv}} = 163$

Interface treatment

Interface thickness parameter:

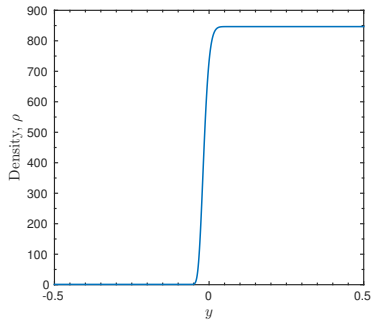
$$\delta = 0.08\lambda$$

Normalized distance from interface:

$$d = \frac{\delta + y(x)_{interface} - y}{2\delta}$$

Volume fraction:

$$y_0 = \begin{cases} 1 \\ \exp \left(\log (10^{-16}) |d|^8 \right) \\ 0 \end{cases}$$



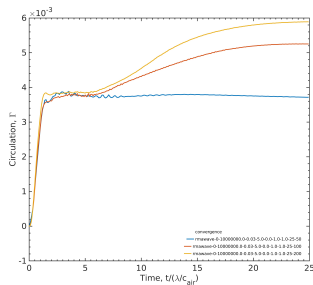
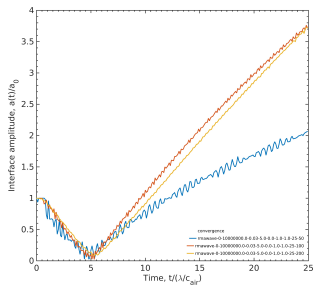
Radiation Pressure

$$P_{net} = \frac{\Delta p_a}{2} \left[1 - \frac{c_w}{c_a} + \frac{(\rho c)_a - (\rho c)_w}{(\rho c)_a (\rho c)_w} \right] \text{ Beyer (1974)}$$

Stress failure in the lungs:

Rabbit lungs under transmural pressure: $\approx 5.2 \text{ kPa}$ (West *et al.*, 1991);

Convergence tests: Compression wave



50 pts / λ ,

100 pts / λ

200 pts / λ